Proceedings of IMECE2006
2006 ASME International Mechanical Engineering Congress & Exposition
November 5-10, 2006, Chicago, Illinois, USA

IMECE2006-13792

NUMERICAL SIMULATION OF DIRECT METAL LASER SINTERING OF SINGLE-COMPONENT POWDER ON TOP OF SINTERED LAYERS

Bin Xiao and Yuwen Zhang
Department of Mechanical and Aerospace Engineering
University of Missouri-Columbia
Columbia, MO 65211
zhangyu@missouri.edu

ABSTRACT

A three dimensional model describing melting and resolidification of direct metal laser sintering of loose powders on top of sintered layers with a moving Gaussian laser beam is developed. Natural convection in the liquid pool driven by buoyancy and Marangoni effects is taken into account. A temperature transforming model is employed to model melting and resolidification in the laser sintering process. The continuity, momentum, and energy equations are solved using a finite volume method. Effects of dominant processing parameters including number of the existing sintered layers underneath, laser scanning velocity and initial porosity on the sintering process are investigated.

INTRODUCTION

Selective laser sintering (SLS) is a rapid prototyping/manufacturing technique that allows generating complex 3-D parts by fusing powdered material layer by layer [1-4]. During the SLS process, a thin powder layer is laser-scanned to fuse the two-dimensional slice to an underlying solid piece, which consists of a series of stacked and fused two-dimensional slices. After laser scanning, a fresh powder layer is spread and the scanning process is repeated. SLS is a complex process that requires further understanding of the physical mechanisms. Some heat conduction models have been developed to reveal the influence of processing conditions for the laser induced heating process in the past. Cheng and Kar [5] conducted a theoretical study for the densification of ceramic coating processed with a moving laser beam. A three dimensional quasi-steady state heat conduction model was developed by applying the Fourier integral transform method. An approximate expression for temperature distribution was also presented and its results are found to be in good agreement with the exact solutions within a limited region around the laser spot. Li et al. [6] modeled the laser melting problem of ceramic materials. A 3-D quasi-steady state heat conduction equation was solved by applying the Green function method, and the singularities associated with the numerical integration are treated using a linear interpolation method. The predicted results from the model using the volumetric heating source and surface heating source are compared with experimental data. Xie and Kar [7] analyzed a one-dimensional heat conduction problem to investigate the melting rate during laser materials processing. The problem was solved approximately to obtain a correlation among melt depth, power density, and laser irradiation time. Based on this correlation, the dynamics of melting, a relationship between the melt depth and power density and an average melting velocity are expressed by simple analytic formulas. The times to reach the melting and boiling temperatures at the surface of the workpiece are also obtained.

The fluid flow within the melt pool is mainly driven by surface tension and buoyancy forces, which play important roles in the temperature distribution and the shape of the liquid pool. Numerical studies of heat transfer and fluid flow in laser-induced melt pool during laser welding and cladding have been carried out in the past. Chan et al. [8] analyzed a transient behavior of heat transfer and fluid flow driven by surface tension on a stationary laser heating process. The effects of various dimensionless parameters on surface temperature, melted pool and cooling rate were studied. Kou and Wang [9] developed a 3-D convection model for the case where the workpiece is moving with respect to the laser beam. Fluid flow driven by buoyancy force and surface tension gradient was considered. The model demonstrated that the surface tension-temperature coefficient can significantly affect both the convection pattern and the penetration of laser melted pool. Li et al. [10] studied the convection-diffusion phase change process during laser melting of ceramic materials. Results by pure heat conduction model, heat conduction model incorporating latent heat of fusion and model involving both

latent heat of fusion and fluid were compared. They demonstrated that the best prediction accuracy for the melt/solid interfaces can be achieved by considering both the latent heat of fusion and fluid flow in the molten pool.

Melting and resolidification are the mechanisms for laser sintering of metal sintering of metal powders to form a layer of part and bond different layers together to form functional part. During metal SLS process, when the laser beam scans and melts a row of powder particles, the melted powder grains stick to each other via surface tension forces, thereby forming a series of spheres with diameters approximately equal to the diameter of the laser beam; this is referred to as balling phenomena. In order to overcome the balling phenomenon, several methods including melting of low-melting point powder in a two-component metal powders system [11-12], partial melting of single-component metal powders [13-15] are developed. The parts produced by partial melting of single-component or two-component metal powders usually are not fully densified and need time-consuming post processing. In order to eliminate the above limitation, direct metal laser sintering (DMLS) technique [16-19] has been developed in the recent years. By applying lower scanning velocity and high laser intensity with protection gas to fully melt each single track, the entire track of the laser scanning can be completely molten without forming spherical structure [16, 18].

The distinctive feature of DMLS is that it is always accompanied by the shrinkage due to the significant density change, which in turn considerably affects the temperature distribution and the shape of liquid pool. Xiao and Zhang [20] have established a theoretical model for DMLS in a semi-infinite powder bed, and the principal character of heat transfer and fluid flow are explored and parametric effects on the sintering process are analyzed. However, in practice, DMLS is a layer-by-layer process by which the sintering process occurs in a fresh loose powder layer on top of multiple sintered layers. For better understanding the influences of the processing parameters on the pool dynamics and geometry as well as surface temperature distribution, the convective heat transfer and fluid flow during DMLS of loose powder on top of existing sintered layer are analyzed numerically in the present study. The effects of shrinkage, laser scanning velocity and the number of existing sintered layers on the sintering process are investigated.

NOMENCLATURE

C	=	dimensionless heat capacity, $\rho c/(\rho c)_\ell$
c	=	specific heat (J/kg-K)
b	=	source term
B	=	dimensionless source term
g	=	gravitational acceleration (m/s^2)
h	=	convective heat transfer coefficient (W/m^2-K)
$h_{s\ell}$	=	latent heat of melting (J/kg)
k	=	thermal conductivity (W/m-K)
N_i	=	dimensionless moving laser beam intensity, $\alpha_a q_0/[\pi R k_l (T_f - T_i)]$
N_R	=	radiation number, $\varepsilon_e \sigma (T_f - T_i)^3 R/k_\ell$
N_t	=	temperature ratio, $T_f/(T_f - T_i)$
p	=	pressure (N/m^2)
P	=	dimensionless pressure, $pR^2/(\rho\alpha_\ell^2)$
q_0	=	laser power (W)
R	=	radius of the laser beam (m)
s	=	location of the melt/solid interface (m)
s_0	=	location of surface (m)
S	=	dimensionless location of the melt/solid interface, s/R
S_0	=	dimensionless location of surface, s_0/R
T	=	temperature (K)
t	=	time (s)
u_b	=	scanning velocity of the laser beam (m/s)
U_b	=	dimensionless scanning velocity of laser beam, $u_b R/\alpha_\ell$
$\mathbf{v}$	=	velocity vector, $u\,\mathbf{i}+v\,\mathbf{j}+w\,\mathbf{k}$ (m/s)
$\mathbf{V}$	=	dimensionless velocity vector, $\mathbf{v}R/\alpha_\ell$
V	=	volume (m^3)
w_s	=	velocity induced by shrinkage (m/s)
W_s	=	dimensionless velocity induced by shrinkage, $w_s R/\alpha_\ell$
x, y, z	=	coordinates (m)
X, Y, Z	=	dimensionless coordinates, $(x, y, z)/R$

Greek symbol

α	=	thermal diffusivity (m^2/s)
α_a	=	absorptivity
θ	=	dimensionless temperature
δT	=	one-half of phase change temperature range (K)
$\delta\theta$	=	one-half of dimensionless phase change temperature range, $\delta T/(T_f - T_i)$
ε	=	initial porosity (volume fraction of void), $V_g/(V_g + V_s)$
ε_e	=	emissivity of surface
μ	=	dynamic viscosity (kg/m-s)
ρ	=	density (kg/m^3)
σ	=	Stefan-Boltzman constant (5.67×10^{-8} W/m^2-K^4)
τ	=	dimensionless time, $\alpha_\ell t/R^2$
Δ_s	=	dimensionless thickness of the loose powder layer

Subscripts

eff	=	effective

g	=	gas
ℓ	=	liquid
f	=	fusion
p	=	powder material
s	=	solid

PHYSICAL MODELS

Problem statement

Figure 1 shows the direct metal laser sintering process of a loose powder layer on top of multiple previously sintered layers under a moving circular Gaussian laser beam at a constant scanning speed, , along the positive x-direction. A fraction of the laser power is absorbed by the powders and leads to the formation of a melt pool. After the laser source moves away, the liquid pool cools and resolidifies to form the fully densified part. The problem under consideration is a typical moving heat source problem [21]. Since the size of heat source (in the order of mm or less) is much smaller than the size of the powder bed, the sintering process appears to be quasi-steady state from the standpoint of the observer located in and traveling with the heat source [22-24].

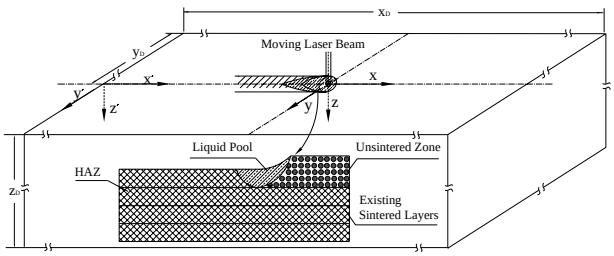

Fig. 1 Physical model for metal laser sintering on top of sintered layers

Governing equations

A temperature transforming model using a fixed grid method [25] is employed to describe the melting and resolidification during laser sintering. This model assumes that the melting and solidification occur over a range of phase change temperature, and it can also be successfully applied to phase change problems at a fixed melting point. Due to axisymmetry with respect to the center plan (y =0), the velocity and temperature fields were computed on only half of the domain (y >0). Since the molten pool moves with the laser beam, the problem is more conveniently studied in a reference frame moves with the laser beam. The governing equations in the moving reference frame (x,y,z) can be expressed as following [26]:

$$\frac{\partial \rho}{\partial t}+\frac{\partial}{\partial x}(\rho u)+\frac{\partial}{\partial y}(\rho v)+\frac{\partial}{\partial z}(\rho w)=0 \tag{1}$$

$$\frac{\partial}{\partial t}(\rho u)+\frac{\partial}{\partial x}\left[\rho u(u-u_b)\right]+\frac{\partial}{\partial y}(\rho uv)+\frac{\partial}{\partial z}\left[\rho u(w+w_s)\right]$$
$$=-\frac{\partial p}{\partial x}+\frac{\partial}{\partial x}(\mu\frac{\partial u}{\partial x})+\frac{\partial}{\partial y}(\mu\frac{\partial u}{\partial y})+\frac{\partial}{\partial z}(\mu\frac{\partial u}{\partial z}) \tag{2}$$

$$\frac{\partial}{\partial t}(\rho v)+\frac{\partial}{\partial x}\left[\rho v(u-u_b)\right]+\frac{\partial}{\partial y}(\rho vv)+\frac{\partial}{\partial z}\left[\rho v(w+w_s)\right]$$
$$=-\frac{\partial p}{\partial y}+\frac{\partial}{\partial x}(\mu\frac{\partial v}{\partial x})+\frac{\partial}{\partial y}(\mu\frac{\partial v}{\partial y})+\frac{\partial}{\partial z}(\mu\frac{\partial v}{\partial z}) \tag{3}$$

$$\frac{\partial}{\partial t}(\rho w)+\frac{\partial}{\partial x}\left[\rho w(u-u_b)\right]+\frac{\partial}{\partial y}(\rho wv)+\frac{\partial}{\partial z}\left[\rho w(w+w_s)\right]$$
$$=-\frac{\partial p}{\partial z}+\frac{\partial}{\partial x}(\mu\frac{\partial w}{\partial x})+\frac{\partial}{\partial y}(\mu\frac{\partial w}{\partial y})+\frac{\partial}{\partial z}(\mu\frac{\partial w}{\partial z})+\rho g\beta(T-T_f) \tag{4}$$

$$\frac{\partial}{\partial t}(\rho cT)+\frac{\partial}{\partial x}\left[\rho cT(u-u_b)\right]+\frac{\partial}{\partial y}(\rho cvT)+\frac{\partial}{\partial z}\left[\rho cT(w+w_s)\right]$$
$$=\frac{\partial}{\partial x}\left(k\frac{\partial T}{\partial x}\right)+\frac{\partial}{\partial y}\left(k\frac{\partial T}{\partial y}\right)+\frac{\partial}{\partial z}\left(k\frac{\partial T}{\partial z}\right) \tag{5}$$
$$-\left[\frac{\partial}{\partial t}(\rho b)+\frac{\partial}{\partial x}\left[\rho b(u-u_b)\right]+\frac{\partial}{\partial y}(\rho bv)+\frac{\partial}{\partial z}\left[\rho b(w+w_s)\right]\right]$$

As porosity equals to zero within the melt pool after melting, the shrinkage velocity of the melting zone can be determined in the moving coordinate system [23]:

$$w_s=\begin{cases}0 & z>s\\ \varepsilon\left(\dfrac{\partial s}{\partial t}-u_b\dfrac{\partial s}{\partial x}\right) & z<s\end{cases} \tag{6}$$

By applying temperature transforming model, the effective heat capacity of the powder bed can be expressed as

$$c=\begin{cases}c_s & T<T_f-\delta T\\ c_m+\dfrac{h_{s\ell}}{2\delta T} & T_f-\delta T\le T\le T_f+\delta T\\ c_\ell & T>T_f+\delta T\end{cases} \tag{7}$$

and in the eq. (5) is defined as

$$b=\begin{cases}0 & T<T_f-\delta T\\ \dfrac{h_{s\ell}}{2} & T_f-\delta T\le T\le T_f+\delta T\\ h_{s\ell} & T>T_f+\delta T\end{cases} \tag{8}$$

The thermal conductivity in eq. (5) in the mushy zone can be assumed as a linear function of temperature, i.e.,

$$k=\begin{cases}k_{eff} & T<T_f-\delta T\\ k_{eff}+\dfrac{k_\ell-k_{eff}}{2\delta T}\left(T-T_f+\delta T\right) & T_f-\delta T\le T\le T_f+\delta T\\ k_\ell & T>T_f+\delta T\end{cases} \tag{9}$$

where k_{eff} is the effective thermal conductivity of the unsintered powder bed. It can be calculated using the empirical correction proposed by Hadley [27].

$$k_{eff} = k_g(1-\alpha_0)\frac{\varepsilon f_0 + (k_p/k_g)(1-\varepsilon f_0)}{1-\varepsilon(1-f_0)+(k_p/k_g)\varepsilon(1-f_0)} + \alpha_0\frac{2(k_p/k_g)^2(1-\varepsilon)+(1+2\varepsilon)(k_p/k_g)}{(2+\varepsilon)(k_p/k_g)+1-\varepsilon} \quad (10)$$

where

$$f_0 = 0.8 + 0.1\varepsilon \quad (10a)$$

$$\log\alpha_0 = \begin{cases} -4.898\varepsilon & 0 \le \varepsilon \le 0.0827 \\ -0.405 - 3.154(\varepsilon - 0.0827) & 0.0827 \le \varepsilon \le 0.298 \\ -1.084 - 6.778(\varepsilon - 0.298) & 0.298 \le \varepsilon \le 0.580 \end{cases} \quad (10b)$$

At the solid-liquid interface or in the mushy region, the velocities are zero. A commonly used procedure is to prescribe a fluid viscosity that is equal to the liquid viscosity in the liquid region and increases gradually over the mushy region to a large value in the solid. Therefore the viscosity is expressed as

$$\mu = \begin{cases} N & T < T_f - \delta T \\ \mu_\ell + \dfrac{\mu_\ell - N}{2\delta T}\left(T - T_f - \delta T\right) & T_f - \delta T \le T \le T_f + \delta T \\ \mu_\ell & T > T_f + \delta T \end{cases} \quad (11)$$

Boundary conditions

The boundary condition at the top surface ($z = s_0$) is

$$-\frac{q_0}{\pi R^2}\exp\left(-\frac{x^2+y^2}{R^2}\right) + h(T - T_\infty) + \sigma_e\varepsilon(T^4 - T_\infty^4) = -k\left(\frac{\partial T}{\partial z}\right)_{z=s_0} \quad (12)$$

where R is the radius of the Gaussian laser beam.

To model the Marangoni convection due to temperature gradients at the top surface, we balance the shear force and surface tension at the free surface

$$\mu\left(\frac{\partial \mathrm{v}_{s_1}}{\partial n} + \frac{\partial \mathrm{v}_n}{\partial s_1}\right) = \frac{\partial\gamma}{\partial T}\frac{\partial T}{\partial s_1} \quad (13)$$

$$\mu\left(\frac{\partial \mathrm{v}_{s_2}}{\partial n} + \frac{\partial \mathrm{v}_n}{\partial s_2}\right) = \frac{\partial\gamma}{\partial T}\frac{\partial T}{\partial s_2} \quad (14)$$

where v_s and v_n in Eq. (13) are the tangential and normal velocity components at the heating surface. The subscripts of v_s, "1" and "2" represent the two tangential directions.

The boundary of pressure at the surface of the molten pool is assumed to be the atmospheric pressure, and the pressure at the liquid-solid interface is determined by Laplace-Young Equation.

$$p = p_\infty, \qquad z = s_0 \quad (15)$$

$$p_\ell = p_v - \frac{2\sigma}{r_{eff}} = p_\infty - \frac{2\sigma}{r_{eff}}, \qquad z = s \quad (16)$$

At the bottom surface ($z = z_{\max}$), the boundary condition for velocity and temperature are as follows:

$$u = v = w = 0 \quad (17)$$

$$-k\frac{\partial T}{\partial z} = h(T - T_\infty) \quad (18)$$

The symmetric conditions at the center surface ($y = 0$) are valid:

$$v = 0 \quad (19)$$

$$\frac{\partial u}{\partial y} = \frac{\partial w}{\partial y} = \frac{\partial T}{\partial y} = 0 \quad (20)$$

At side surface ($y = y_{\max}$), the boundary conditions are

$$u = v = w = 0 \quad (21)$$

$$-k\frac{\partial T}{\partial y} = h(T - T_\infty) \quad (22)$$

At $x = -x_{\max}$ (far ahead of the heat source):

$$u = v = w = 0 \quad (23)$$

$$T = T_i \quad (24)$$

At $x = x_{\max}$ (far behind the heat source):

$$u = v = w = 0 \quad (25)$$

$$\frac{\partial T}{\partial x} = 0 \quad (26)$$

Dimensionless governing equations

Introducing the following dimensionless variables

$$(X,Y,Z) = \frac{(x,y,z)}{R}, (U,V,W,U_b) = \frac{(u,v,w,u_b)R}{\alpha_\ell}, S = \frac{s}{R},$$

$$\tau = \frac{\alpha_\ell t}{R^2},\ \theta = \frac{T - T_f}{T_f - T_i}, \delta\theta = \frac{\delta T}{T_f - T_i},\ C = \frac{\rho c}{(\rho c)_l},\ C_{s\ell} = \frac{(\rho c)_s}{(\rho c)_\ell},$$

$$B = \frac{b}{c_\ell(T_f - T_i)},\ K = \frac{k}{k_\ell},\ K_{eff} = \frac{k_{eff}}{k_\ell}, \mathrm{Pr} = \frac{\mu}{\rho\alpha_\ell},\ \delta\theta = \frac{\delta T}{T_f - T_i}$$

$$St = \frac{c_\ell(T_f - T_i)}{h_{s\ell}}, ,\ P = \frac{pR^2}{\rho\alpha_\ell^2},\ Ra = \frac{g\beta R^3(T_f - T_i)}{\nu_\ell\alpha_\ell} \quad (27)$$

The governing equations can be rewritten as

$$\frac{\partial U}{\partial X} + \frac{\partial V}{\partial Y} + \frac{\partial W}{\partial Z} = 0 \quad (28)$$

$$\frac{\partial U}{\partial\tau} + \frac{\partial[U(U-U_b)]}{\partial X} + \frac{\partial(UV)}{\partial Y} + \frac{\partial[U(W+W_s)]}{\partial Z} = -\frac{\partial P}{\partial X} + \frac{\partial}{\partial X}\left(\mathrm{Pr}\frac{\partial U}{\partial X}\right) + \frac{\partial}{\partial Y}\left(\mathrm{Pr}\frac{\partial U}{\partial Y}\right) + \frac{\partial}{\partial Z}\left(\mathrm{Pr}\frac{\partial U}{\partial Z}\right) \quad (29)$$

$$\frac{\partial V}{\partial\tau} + \frac{\partial[V(U-U_b)]}{\partial X} + \frac{\partial(VV)}{\partial Y} + \frac{\partial[V(W+W_s)]}{\partial Z} = -\frac{\partial P}{\partial Y} + \frac{\partial}{\partial X}\left(\mathrm{Pr}\frac{\partial V}{\partial X}\right) + \frac{\partial}{\partial Y}\left(\mathrm{Pr}\frac{\partial V}{\partial Y}\right) + \frac{\partial}{\partial Z}\left(\mathrm{Pr}\frac{\partial V}{\partial Z}\right) \quad (30)$$

$$\frac{\partial W}{\partial\tau} + \frac{\partial[W(U-U_b)]}{\partial X} + \frac{\partial(WV)}{\partial Y} + \frac{\partial[W(W+W_s)]}{\partial Z} = -\frac{\partial P}{\partial Z} + \frac{\partial}{\partial X}\left(\mathrm{Pr}\frac{\partial W}{\partial X}\right) + \frac{\partial}{\partial Y}\left(\mathrm{Pr}\frac{\partial W}{\partial Y}\right) + \frac{\partial}{\partial Z}\left(\mathrm{Pr}\frac{\partial W}{\partial Z}\right) + \mathrm{Ra}\,\mathrm{Pr}\,\theta \quad (31)$$

$$\frac{\partial(C\theta)}{\partial\tau} + \frac{\partial[C\theta(U-U_b)]}{\partial X} + \frac{\partial(C\theta V)}{\partial Y} + \frac{\partial[C\theta(W+W_s)]}{\partial Z} = \frac{\partial}{\partial X}(K\frac{\partial\theta}{\partial X}) + \frac{\partial}{\partial Y}(K\frac{\partial\theta}{\partial Y}) + \frac{\partial}{\partial Z}(K\frac{\partial\theta}{\partial Z}) - \left[\frac{\partial B}{\partial\tau} + \frac{\partial[(U-U_b)B]}{\partial X} + \frac{\partial(VB)}{\partial Y} + \frac{\partial[(W+W_s)B]}{\partial Z}\right] \quad (32)$$

where

$$W_s = \begin{cases} 0 & Z \geq S \\ \varepsilon\left(\dfrac{\partial S}{\partial \tau} - U_b \dfrac{\partial S}{\partial X}\right) & Z < S \end{cases} \quad (33)$$

$$\mathrm{Pr} = \begin{cases} N & \theta < -\delta\theta \\ \mathrm{Pr}_\ell + \dfrac{(\mathrm{Pr}_\ell - N)}{2\delta\theta}(\theta - \delta\theta) & -\delta\theta \leq \theta \leq \delta\theta \\ \mathrm{Pr}_\ell & \theta > \delta\theta \end{cases} \quad (34)$$

$$C = \begin{cases} C_{s\ell} & \theta < -\delta\theta \\ \dfrac{1}{2}(1 + C_{s\ell}) + \dfrac{1}{2St\delta\theta} & -\delta\theta \leq \theta \leq \delta\theta \\ 1 & \theta > \delta\theta \end{cases} \quad (35)$$

$$K = \begin{cases} K_{eff} & \theta < -\delta\theta \\ K_{eff} + \dfrac{(1 - K_{eff})}{2\delta\theta}(\theta + \delta\theta) & -\delta\theta \leq \theta \leq \delta\theta \\ 1 & \theta > \delta\theta \end{cases} \quad (36)$$

$$B = \begin{cases} 0 & \theta < -\delta\theta \\ \dfrac{1}{2St} & -\delta\theta \leq \theta \leq \delta\theta \\ \dfrac{1}{St} & \theta > \delta\theta \end{cases} \quad (37)$$

The boundary condition Eq. (12) written in dimensionless form is as follows,

$$-K\frac{\partial\theta}{\partial Z} = N_i \exp\left[-X^2 - Y^2\right] - N_R\left[(\theta + N_t)^4 - (\theta_\infty + N_t)^4\right] - B_i(\theta - \theta_\infty) \quad Z = S_0(X,Y) \quad (38)$$

The dimensionless forms of other boundary equations can also be obtained using the dimensionless variables defined in Eq. (26).

NUMERICAL SOLUTIONS

The fabrication of functional part is relying on a layer-by-layer SLS process. The newly sintered layer should integrate tightly with the existing layers underneath for strong mechanical properties. The melting/resolidification problem defined by eqs. (28)– (32) is a steady-state, three-dimensional, nonlinear problem. Since the locations of the solid-liquid interface and the heating surface are unknown a priori, a false transient method is employed to locate various interfaces. Steady-state solution is obtained when the temperature distribution and locations of various interfaces do not vary with the false time. Equations (28)– (32) with the false transient term can be solved by the finite volume method [28]. The computational domain is the whole powder bed and a block-off technique [28] is employed to simulate the existence of the empty space created by shrinkage of the powder bed after melting. The density and thermal conductivity in the empty space are set to be zero.

The governing equations and boundary conditions formulated in eqs. (28)– (32) and eq. (38) were discretized and solved using the SIMPLEC algorithm [28]. The convection and diffusion terms were discretized using the power-law scheme. The boundary conditions are merged into energy and momentum equations for the appropriate nodes using additional source term method [27]. A non-uniform 122×52×52 (in the X, Y, Z directions, respectively) grid number is used in computation and the false time step is 0.001. A fine grid within the melt pool and coarse grid in the unsintered region were used. The iterative procedure was continued until the following convergence criterion was satisfied:

$$\frac{\sum_P \left|\phi - \phi^{old}\right|}{\sum_P |\phi|} < 0.001 \quad (39)$$

where $\sum_P$ denotes summation overall grid points and ϕ is the variables being computed, e.g., U , V , W and T .

The laser intensity and scanning velocity should ensure to obtain the ideal sintering depth which is beyond the bottom surface of the loose powder layer. To obtain the expected sintering depth, the optimum combination of dimensionless laser beam intensity and scanning velocity is required. Therefore, the dimensionless laser power intensity is increased in small increments in order to obtain the expected sintering depth when the sintering depth does not move down. The computation can be stopped when 50% overlap between HAZ and existing sintered layers underneath.

RESULTS AND DISCUSSIONS

The developed computer program is first used to simulate laser melting of a non-porous 6063 aluminum sheet with a dimension of 229×152×3.2 mm. Figure 2 shows the comparison of the fusion boundary obtained by the present study and experiment conducted by Kou and Wang [9]. The nominal beam power indicated on the Spectra Physics 971 continuous-wave CO_2 laser was 1.3 KW. The travel speed of the workpiece was 4.23 mm/s. The power absorbed by the workpiece was measured calorimetrically. A calorimeter was made of a 38×38 mm square tube of the workpiece material. An 86% heat loss from the surface area irradiated by the laser beam includes those by reflection, radiation and convection.

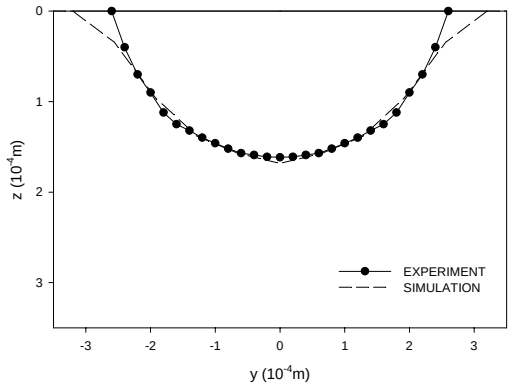

Fig. 2 Comparison of experimental and calculation results for laser fusion of 6063 aluminum sheet

The beam diameter, 0.6 mm, was measured using "split anode method". Detail of the experimental procedure and treatment of the data can be found in Ref. [9]. As Shown in Fig. 2, some discrepancies were observed between the simulated and experimental profiles for the fusion boundaries. The main reason may be due to deviations in the modeled Gaussian model from the actual laser energy distribution. Otherwise, the simulated and measured fusion boundaries are in good agreement with each other.

Numerical calculation is performed for sintering of AISI 304 stainless steel powder in present study. Table 1 lists the material physical properties for AISI 304 [29-30].

Table 1 Thermophysical properties of AISI 304

Nomenclature	Symbol	Unit	Value
Density	ρ_p	kg/m^3	7200
Thermal conductivity	k_p	W/m-K	14.9
Specific heat	c_p	J/kg-K	462.6
Melting point	T_f	K	1670
Latent heat of fusion	$h_{s\ell}$	kJ/kg	247
Viscosity	μ	kg/s-m	0.05
Surface tension at melting point	γ	N/m	1.943
Dependence of surface tension on temperature	$\frac{\partial \gamma}{\partial T}$	N/m K	-4.3×10^{-4}

Figure 3 illustrates the surface temperature distribution of the powder bed at the quasi-steady state ($N=5$). The peak temperature at the powder bed surface is near the trailing edge of the laser beam rather than at the center of the laser beam due to motion of the laser beam. Because the thermal conductivity in the molt pool is much larger than that in the unsintered zone, the temperature changes smoothly in the molten pool but sharply in the unsintered zone near the molt pool. Figure 4 shows the three-dimensional shapes of the powder bed surface, molt pool and HAZ at the same condition of Fig. 3 when $N=1$ and $N=5$. The depths of surface and HAZ decrease with the increasing X in the laser scanning direction Y.

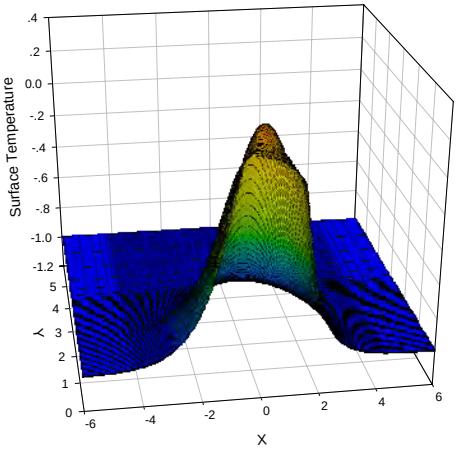

Fig. 3 The temperature distribution at the surface of the powder layer ($\Delta_s=0.4, U_b=0.02, \varepsilon=0.5, N=5$)

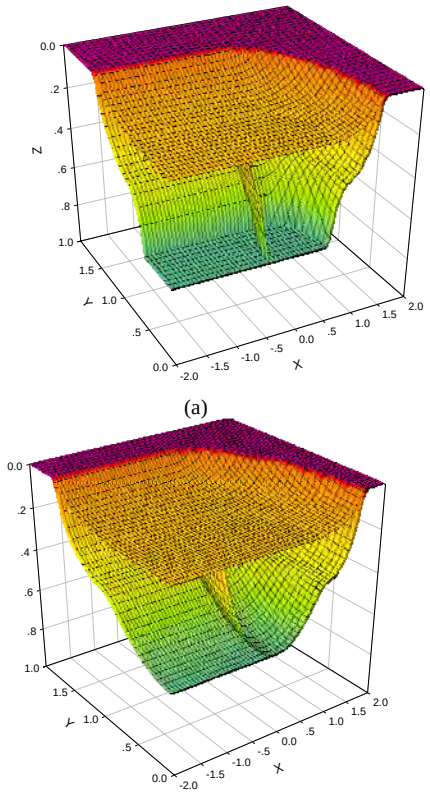

(a)

(b)

Fig. 4 Three-dimensional shape of the HAZ ($\Delta_s=0.4, U_b=0.02, \varepsilon=0.5$), (a) $N=1$; (b) $N=5$

Figure 5(a)-(c) show the velocity vectors in the liquid pool plotted in three different views ($\varepsilon=0.5, N=5$). Since the surface tension is a decreasing function of temperature, i.e., $\partial\gamma/\partial T<0$, the higher surface tension of the cooler liquid metal near the edge of the liquid pool tends to pull the liquid metal away from the center of the liquid pool, where the liquid metal is hotter and the surface tension is lower. Therefore, fluid flow on the surface of liquid pool is radially outward as can be seen in Fig. 5(a). The liquid metal flow is also driven by buoyancy force as illustrated in Fig. 5(b) and 5(c). The hotter liquid metal near the central region of the molten pool flows up to the surface, while the cooler liquid metal near the pool boundary sinks along the melt/solid interface to the bottom of the pool. This circulation of fluid flow induced by the surface tension gradient and buoyancy force is consistent with the typical natural convection pattern found in the literature.

Figure 6(a)-(c) present the temperature contour in the powder bed plotted in three different views ($N=5$). The Marangoni convection (radially outward) at the top surface and the shrinkage phenomenon resulted in a significant amount of heat flows from the hotter region to the colder region especially in the Z direction, which in turn result in a wider and deeper melt pool. Another observation is that the isotherms near the

melting front are more closely spaced compared with those far away from the melt/solid interface.

The effects of shrinkage combined with the scanning velocity of the moving laser beam and the number of the existing sintered layers underneath on the formation of the Heat Affected Zone (HAZ) are investigated. The overlap between the liquid pool and existing sintered layers below are considered in order to bond the newly deposited layer with the existing sintered layers tightly. Figure 7 shows the effect of the dimensionless velocity on the sintering process with only one existing sintered layer. It can be seen from Figure 7(a) that the overlapped region of the liquid pool has reached the bottom of the physical domain when the quasi-steady state is achieved. The higher moving laser beam intensity is needed for the sintering process with higher scanning velocity in order to obtain the same sintering depth. Figure 7(a) also illustrates that, when the scanning velocity increases, the whole melt pool shifts towards the opposite direction of the laser scanning due to the enhanced advection flow caused by the moving of the laser beam relative to the powder bed. Besides, the shapes of HAZ with different velocities are similar but the liquid pool is a litter narrow when the scanning velocity increases as shown in Fig. 7(b). That is due to the fact that the time interaction between the moving laser beam and the powder layer becomes shorter when scanning velocity increases.

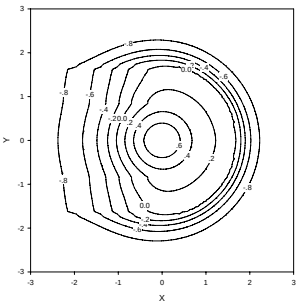

(a)

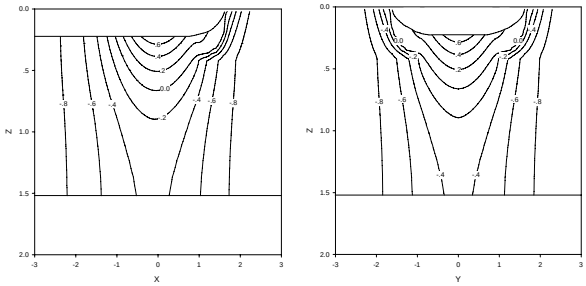

(b) (c)

Fig. 6 Dimensionless temperature contour ($\Delta_s = 0.4, U_b = 0.02, \varepsilon = 0.5, N = 5$), (a) Top view; (b) Longitudinal view at y =0; (c) Cross-sectional view at x =0

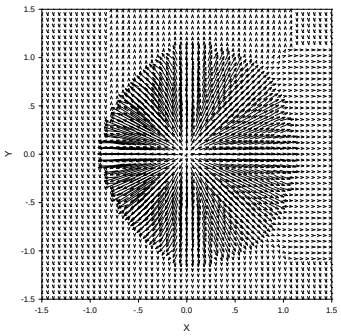

(a)

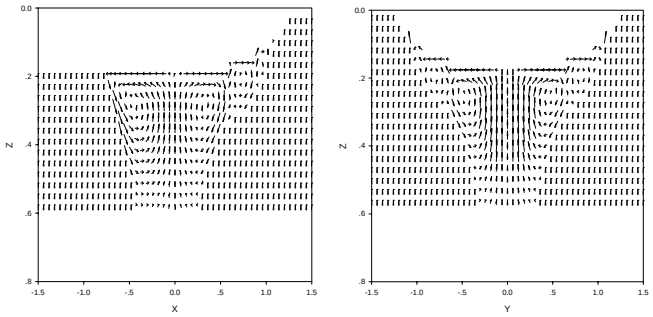

(b) (c)

Fig. 5 Dimensionless velocity vectors ($\Delta_s = 0.4, U_b = 0.02, \varepsilon = 0.5, N = 5$) (a) Top view;(b) Longitudinal view at y =0; (c) Cross-sectional view at x =0

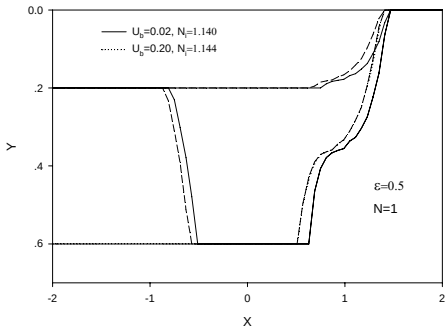

(a)

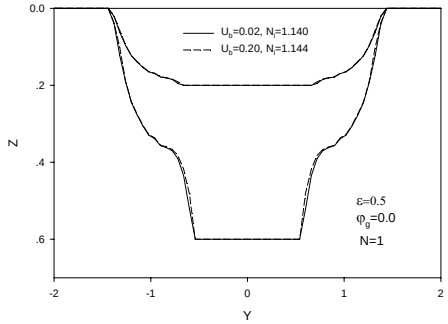

(b)

Fig. 7 Effect of laser intensity and scanning velocity on the sintering process with only one existing sintered layer ($\varepsilon = 0.5, N = 1$), (a) Longitudinal view at y =0; (b) Cross-sectional view at x =0

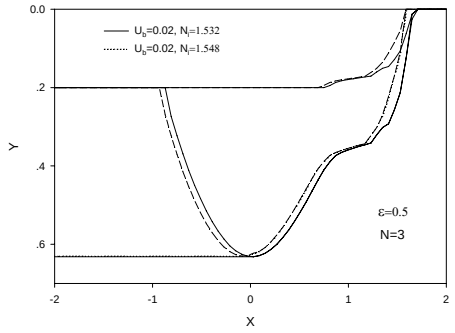

(a)

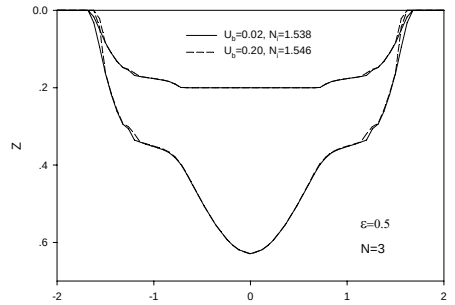

(b)

Fig. 8 Effect of laser intensity and scanning velocity on the sintering process with only one existing sintered layer ($\varepsilon = 0.5,\ N = 3$),

(a) Longitudinal view at y =0; (b) Cross-sectional view at x =0

Figure 8-9 show the effects of the dimensionless velocity on the sintering process with three existing sintered layers ($N = 3$) and five existing sintered layers ($N = 5$). Compared with Figure 7, it can be seen that the laser intensity increases significantly when the number of existed sintered layers underneath the loose powder layer increases. In order to get the desired sintering depth to combine the newly sintered layer with the existing sintered lay, higher laser intensity is need for the case with higher scanning velocity under the same other condition. The liquid pool moves slightly towards the positive direction of the X-direction because of the advection heat flow caused by the moving laser beam. The bottom of the overlapped region of HAZ is not flat since the required overlap between newly sintered layer and existing lay has been achieved before it reaches the bottom surface of the powder bed.

CONCLUSIONS

Three dimensional numerical modeling for direct metal laser sintering on top of sintered layers has been performed. The computer code was validated by comparing the predicted cross-section for the melt/solid interface during laser melting of a non-porous 6063 aluminum sheet with experimental results. The fluid flow greatly influences the temperature distribution and the shapes of liquid pool during laser sintering of single-component metal powder. The optimized combination of the laser intensity and the scanning velocity for the cases with different number of existing sintered layers to achieve the required sintering depth was analyzed. It showed that, when the number of existing sintered layers underneath is increased, higher intensity is needed to achieve required overlap between newly sintered layer and existing layers. As the increase of scanning velocity will shorten the powder/laser interaction time, higher intensity is needed to achieve the required overlap when scanning velocity increases.

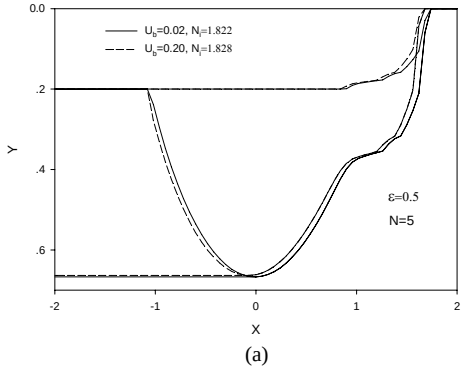

(a)

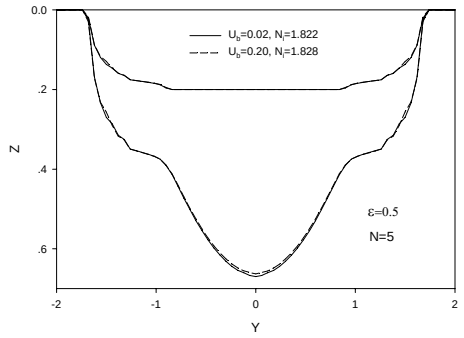

(b)

Fig. 9 Effect of laser intensity and scanning velocity on the sintering process with only one existing sintered layer ($\varepsilon = 0.5,\ N = 5$),

(a) Longitudinal view at y =0; (b) Cross-sectional view at x =0

ACKNOWLEDGEMENT

Support for this work by the Office of Naval Research under grant number N00014-04-1-0303 is gratefully acknowledged.

REFERENCES

[1] Kruth, J. P., 1991, "Material Ingress Manufacturing by Rapid Prototyping Techniques," *Manufacturing Technology CIRP Annals*, Vol. 40, No. 2, pp. 603-614.

[2] Hauser, C., Childs, T. H. C., Dalgarno, K. W. and Eane, R. B., 1999, "Atmospheric Control during Direct Selective Laser Sintering of Stainless Steel 314S Powder,"

Proceedings of Solid Freeform Fabrication Symposium 1999, Austin, TX, pp. 265-272.

[3] Beaman, J. J., Barlow, J. W., Bourell, D. L., Crawford, R. H., Marcus, H. L., and Mcalea, K. P., 1997, *Solid Freeform Fabrication: A New Direction in Manufacturing*, Kluwer Academic Publishers, Dordrecht

[4] Das, S., Beaman, J. J., Wohler, M. and Bourell, D. L., 1998, "Direct Laser Freeform Fabrication of High Performance Metal Components," *Rapid Prototyping Journal*, Vol. 4, No. 3, pp. 112-117.

[5] Cheng, J. and Kar, A., 1997, "Mathematical Model for Laser Densification of Ceramic Coating," *J. of Mater. Sci.*, Vol. 32, pp. 6269-6278.

[6] Li, J.F, Li, L. and Stott, F.H., 2004, "Comparison of Volumetric and Surface Heating Sources in The Modeling of Laser Melting of Ceramic Materials," *Int. J. of Heat Mass Transfer*, Vol. 47, pp. 1159-1174.

[7] Xie, J. and Kar. A., 1996, "Mathematical Modeling of Melting During Laser Materials Processing," *J. Appl. Phys.*, Vol. 81(7), No. 1, pp. 3015-3022.

[8] Chan, C. L., Mazumdar, J. and Chen M. M., 1984, "Two Dimensional Transient Model for Convection in Laser Melted Pool," Metall. Trans. A, Vol. 15A, pp. 2175-2184.

[9] Kou, S. and Wang, Y. H., 1986, "Three Dimensional Convection in Laser Melted Pools," Metall. Trans. A, Vol. 17A, pp. 2265-2270.

[10] Li, J. F., Li, L. and Stott, F. H., 2004, "A Three Dimensional Numerical Model for A Convection-Diffusion Phase Chang Process during Laser Melting of Ceramic Materials," International Journal of Heat & Mass Transfer, Vol. 47, pp 5523-5539.

[11] Bunnell, D.E., Das, S., Bourell, D.L., Beaman, J.B., Marcus, H.L., 1995, "Fundamentals of Liquid Phase Sintering During Selective Laser Sintering," Proceedings of the Solid Freeform Fabrication Symposium, The University of Texas at Austin, Austin, TX, pp. 440-447.

[12] Tolochko, N. K., Mozzharov, S. E., Sobolenko, N. V., Yadroitsev, I. A., Goryushkin, V. I and Dubovets, V. S., "Problems and Prospects of Selective Layer-by-Layer Laser Sintering of powders," Powder Metallurgy and Metal Ceramics, Vol. 34, No. 3-4, pp. 142-145, 1996.

[13] Tolochko, N. K., Mozzharov, S. E., Laoui, T. and Froyen, L., 2003, "Selective Laser Sintering of Single- and Two-Component Metal Powders," Rapid Prototyping Journal, Vol. 9, No. 2, pp 68-78.

[14] Tolochko, N. K., Mozzharov, S. E., Sobolenko, N. V., Khlopkov, Y. V., Yadroitsev, I. A. and Mikhailov, V. B., 1995, "Main Relationship Governing Laser Sintering of Loose Single-Component Metallic Powders," J. Adv. Mat., Vol. 2, No. 2, pp. 151-157.

[15] Agarwala, M., Bourell, D., Beaman, J., Marcus, H. and Barlow, J., 1995, "Direct Selective Laser Sintering of Metals," Rapid Prototyping Journal, Vol. 1, No. 1, pp. 26-36.

[16] Meiners, W., Over, C., Wissenbach, K. and Poprawe, R., 1999, "Directive Generation of Metal Parts and Tools by Selective Laser Powder Remelting," Proceeding of Solid Freeform Fabrication Symposium 1999, pp. 655-661.

[17] Simichi, A., Petzoldt, F. and Pohl, H., 2001, "Direct Metal Laser Sintering: Material Considerations and Mechanisms of Particle Bonding," International Journal of Powder Metallurgy, Vol. 37, No. 2, pp. 49-61.

[18] Morgan, R., Sutcliffe, C.J. et al., 2001, "Experimental Investigation of Nanosecond Pulsed Nd:YAG Laser Re-melted Pre-placed Powder Beds," Rapid Prototyping Journal, Vol. 7, No. 3, pp. 159-172.

[19] Pogson, S.R., Fox, P., Sutcliffe, C.J. and Neill W.O., 2003, "The Production of Copper Parts Using DMLR," Rapid Prototyping Journal, Vol. 9, No. 5, pp. 334-343.

[20] Xiao, B., and Zhang, Y., "Marangoni and Buoyancy Effects on Direct Metal Laser Sintering with a Moving Laser Beam," Numerical Heat Transfer, in review.

[21] Zhang, Y., Faghri, A., 1999, "Melting of a Subcooled Mixed Powder Bed with Constant Heat Flux Heating," Int. J. Heat and Mass Transfer, 42, pp. 775-788.

[22] Chen, T., and Zhang, Y., "Three-Dimensional Simulation of Selective Laser Sintering of a Two-Component Metal Powder Layer with Finite Thickness," ASME J. Manufacturing Science and Engineering, Vol. 128, No. 1, pp. 299-306, 2006.

[23] Xiao, B., and Zhang, Y., "Partial Melting and Resolidification of Metal Powder in Selective Laser Sintering," AIAA J. Thermophysics and Heat Transfer, Vol. 20, 2006, to appear.

[24] Eckert, E. R. G., and Drake, R. M., 1972, Analysis of Heat and Mass Transfer, McGraw-Hill, London.

[25] Cao, Y. and Faghri, A., "A Numerical Analysis of Phase Change Problems Including Natural Convection," ASME J. Heat Transfer, Vol. 112, 1990, pp. 812-816.

[26] Dutta, P., Joshi, J. and Janaswami, R., 1995, "Thermal Modeling of GTAW Process with Non-Axisymmetric Boundary Conditions," Numerical Heat Transfer A, Vol. 27, pp. 499-518.

[27] Hadley, G. R., 1986, "Thermal Conductivity of Packed Metal Powders," Int. J. Heat and Mass Transfer, Vol. 29, pp. 909-920.

[28] Patankar, S. V, 1980, Numerical heat transfer and Fluid Flow, McGraw-Hill, New York.

[29] Kim, W. H., Fan, H. G., Na, S. J., 1997, "Effect of Various Driving Forces on Heat and Mass Transfer in Arc Welding," Numerical Heat Transfer, Part A, Vol. 32, pp. 633-652.

[30] Incropera, F. P., Dewitt, D. P., 2001, Fundamentals of Heat and Mass Transfer, 5th Ed., John Wiley & Sons, Inc., New York.